AIAA SciTech Forum
January 3-7, 2022, San Diego, CA & Virtual
AIAA SCITECH 2022 Forum

10.2514/6.2022-1826

Supersonic transition in a numerically simulated tunnel environment

Hemanth Goparaju*, Yuchen Liu†, Lian Duan‡ and Datta V Gaitonde§
Department of Mechanical and Aerospace Engineering, The Ohio State University, Columbus, Ohio, USA, 43210

Predicting laminar-to-turbulent transition location is vital for the design of high-speed vehicles. This location depends significantly on the nature of disturbances emanating from tunnel walls, which is difficult to characterize experimentally. Freestream disturbances associated with acoustic radiation from turbulent boundary layers developing spatially over interior walls of a supersonic Mach 2.5 channel are numerically generated, and a reduced order model for the freestream disturbances is developed using data-driven techniques. Transition induced by these perturbations is studied on a canonical flat plate, from freestream receptivity to breakdown stages. The most amplified oblique first mode wave interacts with other perturbations in the inlet spectra generating boundary-layer streaks, which is further confirmed by bicoherence analysis. An intermittent high-frequency signature is revealed by wavelet transformation at the boundary-layer edge, which manifests as short wavelength structures over streamwise streaks. Late non-linear stages of transition are characterized by merging turbulent spots and asymmetrically oscillating low-speed streaks closer to the wall. Further, the development of early turbulent regime is accompanied by multi-scale interactions and an emergence of an inertial sub-range.

I. Introduction

Laminar-to-turbulent transition (LTT) estimation is one of the key challenges in designing high speed vehicles. It is vital to understand the physical mechanisms involved in order to be able to accurately predict the transition point. In low disturbance environments, the main route from the laminar to turbulent state, can be summarized into receptivity, eigenmode growth of instabilities, and nonlinear breakdown to turbulence. Receptivity is the process by which freestream disturbances enter the boundary layer. These disturbances grow exponentially (eigenmode growth), and ultimately the laminar state breaks down to a turbulent one. The process leading to this breakdown depends on the initial amplitude and the nature of receptivity [1].

Experimental and numerical efforts complement each other in understanding LTT at high speeds. Transition experiments are typically conducted in conventional (i.e., noisy) tunnels, which have significantly different freestream disturbance signature, leading to different transition mechanisms [2]. Disturbances in the free stream of a conventional supersonic wind tunnel can be broadly classified into acoustic, vortical or entropic waves [3]. At Mach 2.5 and above, freestream disturbances in conventional ground tests may be dominated by acoustic radiation from the tunnel wall [4]. The nature of these tunnel disturbances is difficult to characterize completely [5]. Numerical studies on transition typically involve triggering the most unstable waves, based on linear stability theory, to study their evolution to turbulence [6, 7]. While this methodology provides significant insights into the relevant mechanisms, in a realistic flow there can be many competing phenomena and an accurate prediction of the transition location (corresponding to experiments or free-flight) remains challenging.

Recently, there have been significant efforts to study *natural* transition, with freestream forcing which is either non-deterministic or extracted from experimental measurements. Balakumar and Chou [8] used freestream temporal pressure spectra from experiments of Marineau et al. [9] to study transition on hypersonic blunt nosed configurations. Hader and Fasel [10] and later, Goparaju and Gaitonde [11] studied transition induced by stochastic forcing on a hypersonic flared cone and flat plate respectively, and reported fundamental resonance as a dominant secondary instability mechanism. Dettenrieder et al. [12] examined transition on a hypersonic compression ramp with experimentally informed freestream fluctuations from quiet and noisy tunnels; and reported spanwise non-uniformities in unsteady shear

*Graduate Research Assistant
†Graduate Research Assistant
‡Associate Professor, AIAA Associate Fellow
§Glenn Chair Professor, AIAA Fellow

layer, reattachment shock. While the temporal signature of freestream fluctuations can be obtained from experiments, to completely estimate the tunnel disturbances, information on the wavenumber spectrum is vital, but is not easily accessible.

Significant progress has also been made in characterizing tunnel disturbances and their effects on flight testing [4, 5, 13]. This has led to various DNS studies to investigate the freestream acoustic disturbances from these tunnels, most of which focus on the radiation from spatially developing turbulent boundary layers over flat plates [14–17]. Furthermore, DNS studies from axisymmetric nozzles [18] and rectangular wind tunnels [19, 20] have shown that the radiation intensity from a flat plate boundary layer can be superimposed at the core region of the test-section by combining radiation boundary layers following Laufer's observations [4]. An overview of these studies can be found in Duan et al. [21].

To study the effects of (noisy) tunnel disturbances on LTT, in the current work, a double-walled supersonic channel flow with two independent, spatially evolving flat-plate turbulent boundary layers with an edge Mach number of $M_\infty = 2.5$ is first simulated, which provides freestream acoustic disturbances typical of a conventional supersonic wind tunnel. Next, the role of these disturbances in inducing transition on a test object is studied, providing a realistic estimation of transition process. The current paper is organized as follows. The governing equations and numerical strategies employed are outlined in sec. II. The generation of tunnel disturbances is provided in sec. III. A reduced order representation of this flow field is elucidated in sec. IV, and the transition studies are provided in sec. V, followed by the summary in sec. VI.

II. Governing equations and numerical techniques

The flow governing equations in the current study are the three-dimensional Navier–Stokes equations cast in conservative-law form and are given in Cartesian coordinates as:

$$\frac{\partial U}{\partial t} + \frac{\partial F_j}{\partial x_j} + \frac{\partial F_{vj}}{\partial x_j} = 0, \ (j = 1, 2, 3) \tag{1}$$

The tensor notation (x_1, x_2, x_3) represents the Cartesian coordinates (x, y, z). The vector $\mathbf{U}$ contains five conservative flow variables:

$$\mathbf{U} = [\rho \ \rho u_1 \ \rho u_2 \ \rho u_3 \ e]^T \tag{2}$$

where F_j and F_{vj} are defined as

$$F_j = \begin{Bmatrix} \rho u_j \\ \rho u_1 u_j + p\delta_{1j} \\ \rho u_2 u_j + p\delta_{2j} \\ \rho u_3 u_j + p\delta_{3j} \\ (e + p)u_j \end{Bmatrix} \tag{3}$$

$$F_{vj} = \begin{Bmatrix} 0 \\ -\tau_{1j} \\ -\tau_{2j} \\ -\tau_{3j} \\ -\tau_{jk}u_k - \mathbf{q}_j \end{Bmatrix}, \ (k = 1, 2, 3) \tag{4}$$

The equations of state and transport are:

$$p = \rho RT \tag{5}$$

$$e = \rho(c_v T + 0.5 u_k u_k) \tag{6}$$

$$\tau_{ij} = \mu\left(\frac{\partial u_i}{\partial x_j} + \frac{\partial u_j}{\partial x_i}\right) - \lambda \frac{\partial u_k}{\partial x_k}\delta_{ij}, \ \lambda = \frac{2}{3}\mu \tag{7}$$

$$\mathbf{q}_j = -\kappa \frac{\partial T}{\partial x_j} \tag{8}$$

where c_v is constant with a given γ, and κ can be determined with a constant Prandtl number along with the viscosity coefficient defined by Sutherland's law. The Navier–Stokes equations in Cartesian coordinates (x, y, z, t) are

Parameter	Value	Parameter	Value	Parameter	Value
M_∞	2.5	ρ_∞	0.1 kg/m^3	T_∞	270 K
l	200 mm	Re_∞	4.9×10^6 $/m$	u_∞	823.6 m/s
γ	1.4	Pr	0.72	T_w/T_∞	2.1
R	287.04 Nm/kgK (air)	δ_i	5 mm		

Table 1 Freestream conditions

transformed into body-fitted curvilinear computational domain coordinates (ξ, η, ζ, τ). The conservation equations are non-dimensionalized as: velocity with freestream velocity u_∞, density with freestream density ρ_∞, pressure with $\rho_\infty u_\infty^2$ and time coordinate with l/u_∞ as provided in table 1. All the results presented are in non-dimensional form unless specified.

To simulate the double-walled supersonic channel flow for generating freestream acoustic disturbances, the convective terms are cast in a split form and discretized using a sixth-order accurate central scheme [22–24], whereas a fourth-order central difference scheme is used for both the first and second derivatives in viscous terms. The time integration is performed using a third-order low-storage Runge-Kutta scheme [25]. Two independent, spatially developing single-wall boundary layers are first simulated using the well established recycling/rescaling turbulence inflow generation method [14, 26]; The time series profiles are then extracted from these single-wall simulations and imposed as the inflow boundary conditions for the double-wall case. A detailed analysis of the turbulence generation processes on simulated tunnel walls can be found in Prasad et al. [27].

For the flat plate transition studies, the inviscid Roe fluxes are calculated from a seventh-order weighted essentially non-oscillatory reconstruction of characteristic variables (Balsara and Shu [28]). The stability of the shocks is increased by Ducros [29]-like sensor which locally switches the inviscid fluxes to a low-order Riemann-solver. Sixth-order, compact-central-difference, spectral-like schemes (Lele [30], Visbal and Gaitonde [31]) are employed for discretizing viscous fluxes. Second-order Beam and Warming method [32] in a diagonalized form (Pulliam and Chaussee [33]) is invoked for time marching. A non-dimensional time step of $\Delta t = 1 \times 10^{-4}$ is utilized, and two Newton-like sub-iterations are performed in the implicit scheme at each time step to recover accuracy due to errors introduced by linearization, factorization and explicit updating of the boundary conditions. The appropriate boundary conditions are provided in the subsequent sections.

III. Acoustic disturbances in a two-dimensional supersonic test section

The DNS database used to emulate tunnel disturbances in the current investigation is of a spatially evolving channel flow at Mach 2.5. The channel has a slightly increasing height with an expansion angle of 0.3 deg to account for a growing boundary layer downstream. At the selected expansion angle, the resulting Clauser pressure-gradient parameter is $|\beta| < 0.05$ over the downstream portion of the channel where statistics of turbulent and acoustic fields are evaluated. The small values of the Clauser parameter β in the present simulation may be compared with the range of $0 < \beta < 1.68$ in the simulations of Lee and Sung [34], who investigated the effect of adverse pressure gradient on turbulent boundary layers, designating $\beta = 1.68$ as a strong pressure gradient and the case of $\beta = 0.73$ as a moderate pressure gradient. The above comparison indicates that the pressure gradient effect in the present simulation is relatively insignificant and that a near-equilibrium state should have been reached in the channel-wall turbulent boundary layers. This claim is further supported in the subsequent results wherein we demonstrate a satisfactory agreement between the computed variation in skin friction coefficient C_f as a function of Re_θ and other established results in the literature. By choosing such a double-wall geometry, the effects of surface curvature and pressure gradient in the streamwise direction can be neglected to the leading order, thus avoiding extraneous complexity in the simulation. The freestream and wall parameters are listed in table 1.

To generate the inflow boundary conditions for the double-wall case, two independent, spatially developing single-wall boundary layers are first simulated, and the time series profiles extracted from each single-wall simulation are imposed as the inflow boundary conditions for the turbulent boundary layer developing over either the top or bottom wall of the channel. The computational domain for one of the precursor single-wall DNS and that for the double-wall DNS are shown in fig. 1(a) and fig. 1(b), respectively. The domain size for the double-wall simulations is $(65.0\delta_i, 5.4\delta_i, 11.7\delta_i)$ in the streamwise (x), spanwise (y), and wall-normal (z) directions, where $\delta_i = 4.0mm$ is the inflow boundary layer

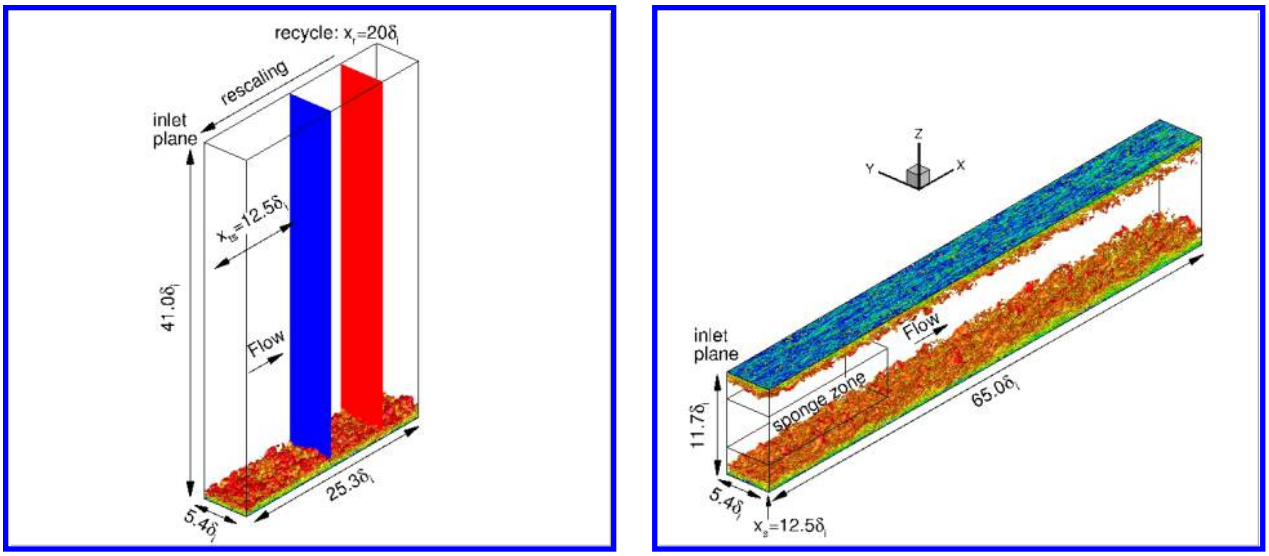

(a) (b)

Fig. 1 Computational domain set up for the DNS case (a) Single wall, and (b) Double wall. An instantaneous flow is shown in the domain visualized by iso-surface of the magnitude of density gradient, $\|\delta\rho\|\delta_i/\rho_\infty = 0.98$, colored by the streamwise velocity component. x_{ts} is the streamwise location where time series data of single-wall are extracted. Sponge zone is marked at the inflow of double-wall domain.

Case	Re_θ	Re_τ	$Re_{\delta 2}$	θ (mm)	H	δ (mm)	z_τ (mm)	u_τ (m s^{-1})
Double Wall	2697	462	1577	0.56	3.8	6.9	0.015	40.5

Table 2 Boundary layer properties at the reference station $x_a/\delta_i = 46.3$ for the double-wall supersonic channel flow.

thickness for the single-wall case. The number of grid points in the streamwise, spanwise, and wall-normal directions are $(1960, 276, 581)$, respectively, corresponding to a grid spacing of $(\Delta x, \Delta y, \Delta z) = (8.9, 5.2, 0.6 - 9.0)$. The nonphysical shocks generated at the channel inlet are damped using a sponge zone near the wall, the details of which are highlighted in Prasad et al. [27]. For reference, table 2 lists the value of the boundary layer parameters at the reference location $x_a/\delta_i = 46.3$ for the double-wall supersonic channel flow, including the momentum thickness θ, shape factor $H = \delta^*/\theta$, boundary layer thickness δ, viscous length z_τ, friction velocity u_τ, and three different Reynolds number parameters, Re_θ, Re_τ, and $Re_{\delta 2}$.

Figure 2(a) compares the van Driest II transformed skin friction coefficient of the current DNS cases to the empirical friction law of Smits et al. [35] and a DNS by Pirozzoli et al. [36] at Mach 2. The van Driest II transformation [37] is used to transform the compressible skin friction to that in an equivalent incompressible flow to allow a comparison with the established skin friction correlations for low-speed flows, specifically,

$$C_{fi} = F_c C_f, \quad Re_{\theta i} = \frac{\mu_\infty}{\overline{\mu}_w} Re_\theta = Re_{\delta 2} \tag{9}$$

where $Re_{\theta i}$ is the Reynolds number based on the momentum thickness of the equivalent incompressible boundary layer, and F_c is the van Driest II scaling factor, given as:

$$F_c = \frac{\overline{T}_w/T_\infty - 1}{\arcsin^2 \alpha}, \quad \alpha = \frac{\overline{T}_w/T_\infty - 1}{\sqrt{\overline{T}_w/T_\infty (\overline{T}_w/T_\infty - 1)}} \tag{10}$$

The incompressible friction law [35] used for comparison is

$$C_{fi} = 0.024 Re_{\theta i}^{-1/4}. \tag{11}$$

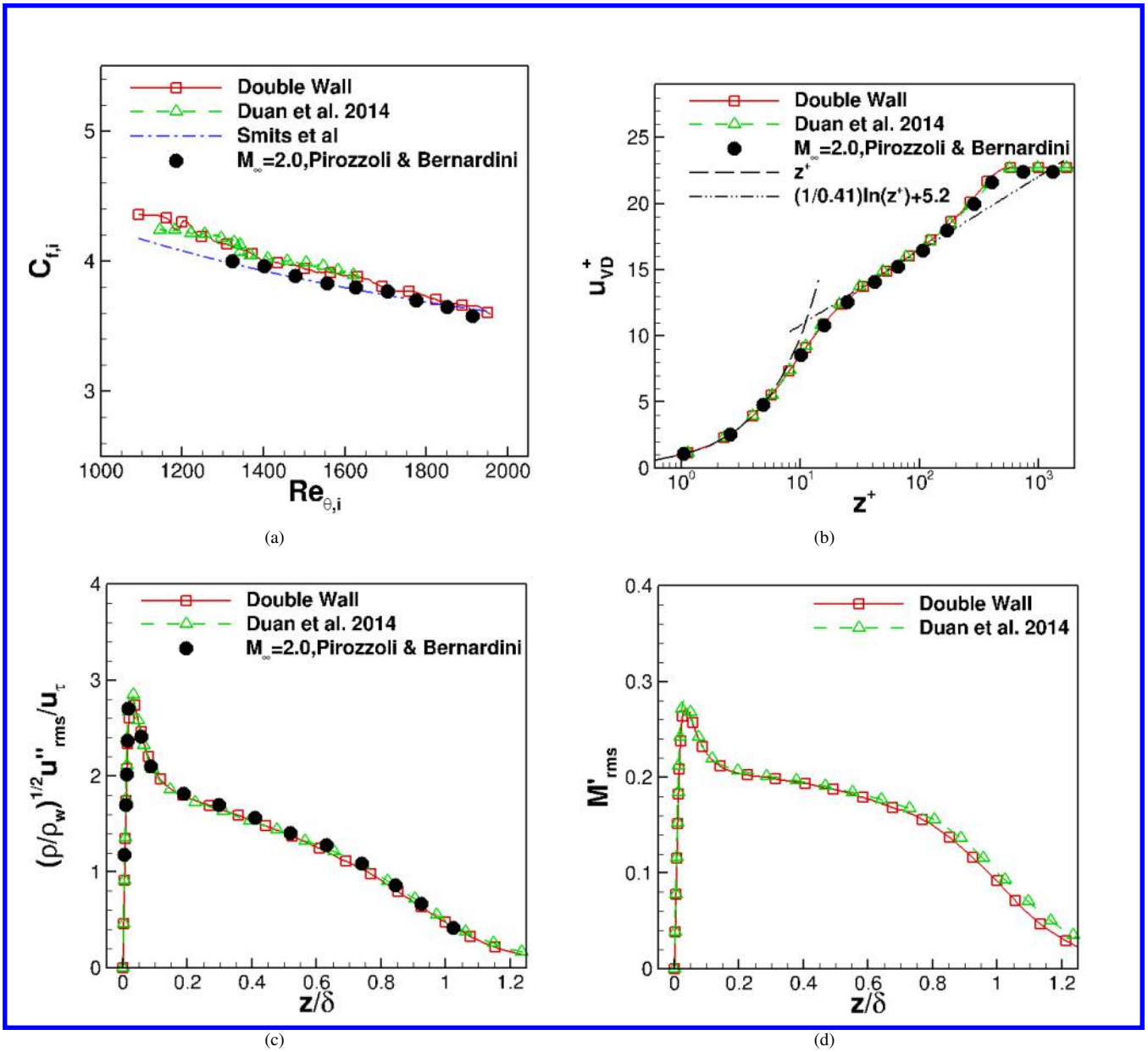

Fig. 2 Validation of Mach 2.5 Double Wall, (a) van Driest II transformed skin friction coefficient, (b) van Driest transformed velocity profile, (c) r.m.s. streamwise velocity fluctuations, and (d) r.m.s. Mach number fluctuations. DNS profiles are selected at the reference location $x_a/\delta_i = 46.3$ for the double-wall case at (b-d). The single-wall case is taken from Duan et al [14] at $M_\infty = 2.5$. Solid symbols denote reference data by Pirozzoli and Bernardini [36] at $M_\infty = 2$.

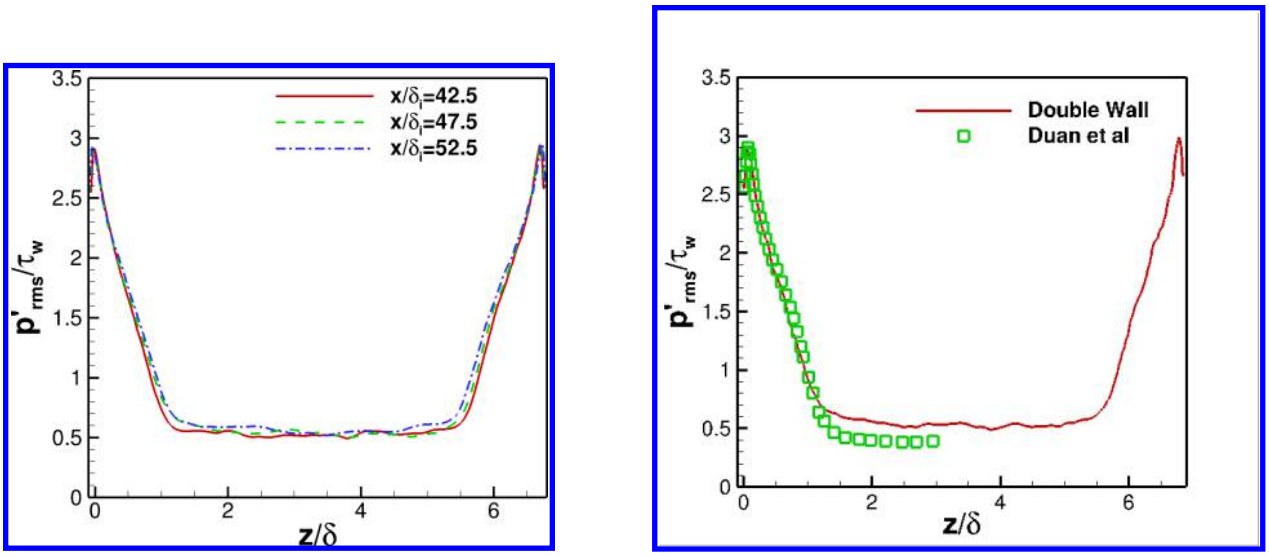

(a) (b)

Fig. 3 (a) **Wall-normal distributions of the normalized r.m.s. pressure fluctuation at selected downstream locations for the double-wall case, and** (b) **Wall-normal profile of r.m.s. pressure fluctuation at the reference location** $x_a/\delta_i = 46.3$**. Solid line: present double wall; square symbol: Duan et al [14].**

The van Driest II transformed skin friction coefficient for the double-wall case matches well with the single-wall case by Duan et al. [14] and also with the above incompressible friction law and the supersonic DNS by Pirozzoli et al. [36].

Figure 2(b) plots the van Driest transformed mean velocity profile, $\overline{U}_{VD} = \frac{1}{u_\tau}\int_0^{\overline{U}} (\overline{T}_w/\overline{T})^{1/2} dU$, at the reference streamwise location for the double-wall DNS case, along with pertinent data from the previous literature. The figure shows that the van Driest transformed velocity profile of the DNS case collapses well with those from the reference datasets. The DNS profiles in the figure show a clearly linear viscous zone, $u^+_{VD} = z^+$, and a logarithmic region where $u_{VD} = 1/\kappa \log(z^+) + C$ with $\kappa = 0.41$ and $C = 5.2$.

Figure 2(c) shows the wall-normal distributions of the normalized, density weighted turbulence intensity [36]. The current DNS case is in good agreement with the data from the existing literature [14, 36]. The Mach number fluctuations, shown in fig. 2(d), are also the same for both the double-wall and single-wall cases, indicating that there is little or no effect of the double-wall configuration on the turbulent fluctuations within the boundary layer.

Figure 3(a) plots the wall-normal profiles of normalized pressure fluctuations at three different streamwise locations, $x/\delta_i = 42.5, 47.5$, and 52.5, respectively. The agreement between all three profiles indicates that both the boundary layer turbulence and the freestream acoustic field have become approximately homogeneous within this downstream portion of the computational box. Figure 3(b) compares the wall-normal distributions of the normalized pressure fluctuation at the reference location. Within the boundary layer, the pressure fluctuations nearly collapse on the single-wall data [14]. In the free stream, however, the fluctuations are $\sqrt{(}2)$ times the single-wall value, or equivalently, the intensity of the freestream acoustic fluctuations for the double-wall case is nearly 2 times that in the single-wall case. This finding is consistent with the observations by Laufer [4], who reported that the acoustic fluctuations radiated from multiple tunnel walls can be superimposed in a mean-square sense and, hence, that the intensity of pressure fluctuations in the core region of the tunnel test section is approximately equal to that radiated from a single tunnel-wall boundary layer multiplied by the number of radiating walls. An analogous result was also obtained for a Mach 6 test section in previously reported DNS simulations [19, 20].

An instantaneous visualization of the database is depicted in fig. 4. Near the walls coherent structures arise, which radiate pressure waves into the center of the test section. Acoustic structures consisting of upward and downward propagating acoustic waves within the freestream region are shown in an instantaneous flow field, where the freestream acoustic field is visualized by the gray contours of the density gradient (fig. 4). The inclination angle of the downward inclined pressure structures radiating from the bottom wall boundary layer is approximately 40°, which is nearly the same as that of the single-wall case [14]. In the next section, the procedure to employ these tunnel disturbances as a source of freestream fluctuations for transition studies is outlined.

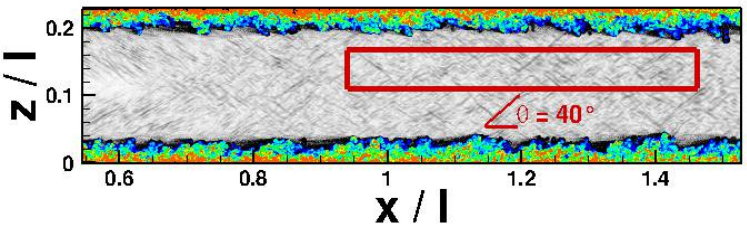

Fig. 4 Numerical schlieren image based on instantaneous flow field in the streamwise wall-normal (x-z) plane. The domain of interest for transition studies is highlighted in the box.

IV. Reduced order representation of tunnel acoustic disturbances

To study the transition induced by tunnel disturbances, the flow features must be effectively captured for specifying appropriate forcing conditions. Here, the focus is on freestream acoustic disturbances radiated by the turbulent structures developed on the tunnel wall shown in fig. 1(b). The effect of the leading edge shock from the test object to the tunnel walls and its further influence on the freestream is ignored. To this end, a sub-domain is isolated based on uniform pressure fluctuations elucidated in fig. 3 and is highlighted in fig. 4. Preliminary analyses showed that the freestream sub-domain extent is not sufficient for breakdown studies. To generalize the database, a modal approach is followed, with a decomposition of the flow field in the sub-domain of fig. 4 represented as in eq. 12.

$$q = \sum_{n=1}^{nf} \hat{q_n} e^{i(k_x x + k_y y + k_z z - \omega t + \phi)} \tag{12}$$

where, q are the field variables, n is the number of modes, (k_x, k_y, k_z) are streamwise, spanwise and wall-normal wavenumbers, ω is the temporal frequency, and ϕ is the phase, where each mode from $n = 1$ to $n = nf$ has an amplitude $\hat{q}_n$.

To determine the number of modes nf, proper orthogonal decomposition (POD) is applied. POD is a data-driven reduced order representation, which provides an optimal basis for variance (energy) of the data as shown in eq. 13.

$$q_n = \sum_{j=1}^{N} a_j(t)\Phi(j), \; R\Phi_j = \lambda_i \Phi \tag{13}$$

where the flow variable q_n is written as a linear combination of eigenfunctions $\Phi(j)$ with coefficients $a_j(t)$. R is the covariance matrix of flow field snapshots and λ_j is the eigenvalue. Here, the ratio $\sum_{j=1}^{r} \lambda_j / \sum_{j=1}^{N} \lambda_j$, denotes the energy captured in r modes. 2500 planar snapshots of pressure, with a time step $\Delta t = 10^{-7} s$, corresponding to the sub-domain highlighted in fig. 4, were averaged and the resulting (mean subtracted) perturbation field was processed with POD. As plotted in fig. 5(a), 90% of the energy is captured in 30 modes. This analysis was repeated for kinetic energy and Chu's energy norm [38] and similar energy distributions were found.

Further, to determine the spectral content of the flow field, dynamic mode decomposition (DMD) is used. DMD provides modal structure, along with associated growth rates, through a best-fit linear operator to the time resolved data [39]. Here, composite DMD [40], where the evolution of all field variables (u, v, w, P, ρ) is considered, has been employed and the corresponding spectral signature is shown in fig. 5(b), capturing 90% of the energy based on POD. Note that CDMD modes occur in pairs and the complex conjugates of the spectra are omitted in the plot for brevity. The frequencies hence obtained from CDMD provides the circular frequencies ω in eq. 12. The pressure modal structure corresponding to the frequency highlighted ($fl/u_\infty = 7.3$) in fig. 5(b) is shown in fig. 5(c). The complementary modal structures of density and velocity satisfy acoustic relations (zero vorticity and entropy), consistent with the observations of Duan et al. [21]. $2D$ FFT analysis on the modal structure in fig. 5(c) extracts the streamwise (k_x) and wall-normal (k_z) wavenumbers as seen in fig. 6(a). For the current analysis, only the most amplified wavenumber pair has been used. To determine the spanwise wavenumber, the (slow) acoustic compatibility equation $(\omega(\mathbf{k}) = \mathbf{u}_\infty \cdot \mathbf{k} - c_\infty ||\mathbf{k}||)$ is invoked, where $(c_\infty, \mathbf{k})$ denotes speed of sound and wavenumber vector, respectively with $||.||$ as the magnitude [12]. Finally, to determine the amplitude of the modes $\hat{q}_n$ in eq. 12, the FFT of pressure signal in the sub-domain is utilized and owing to acoustic nature of the disturbances, the amplitudes of other field variables can be derived, which will be elucidated in the context of transition simulations in the next section.

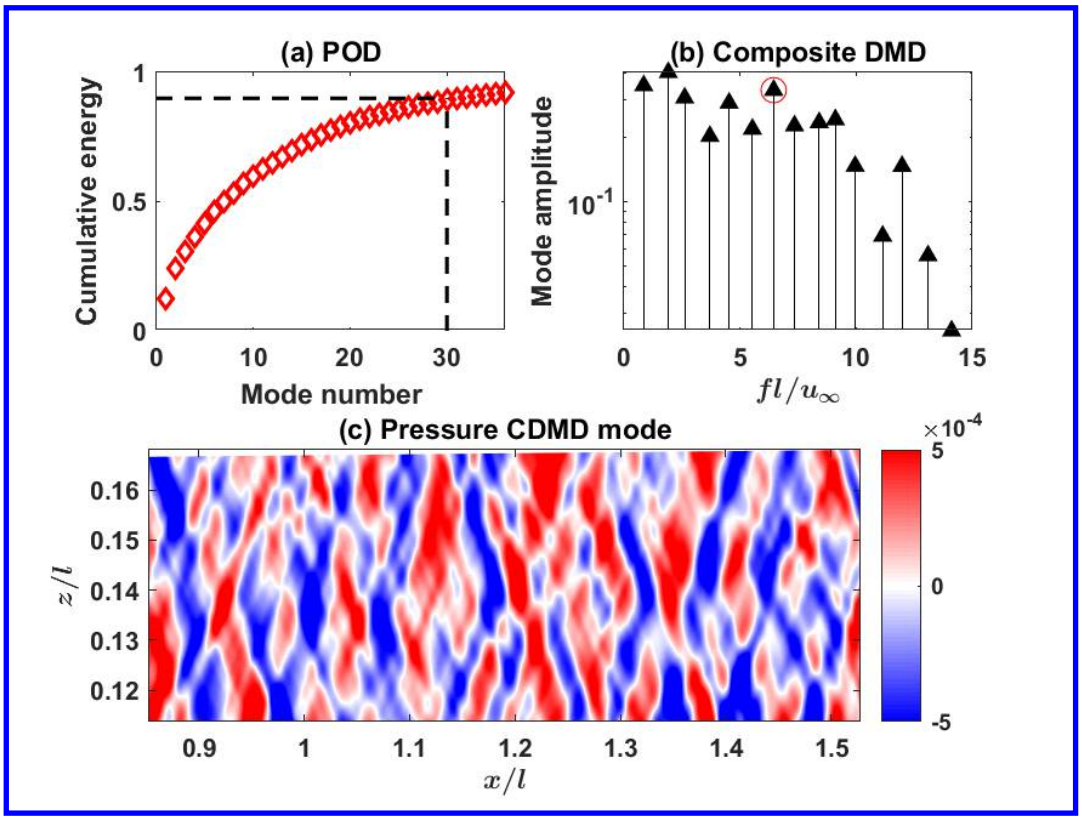

Fig. 5 Reduced order representation of tunnel disturbances. (a) **Cumulative energy of pressure POD modes.** 90% **of energy is captured by** 30 **modes.** (b) **Composite DMD spectra of primitive variables** (c) **Pressure CDMD mode corresponding to the frequency highlighted in** (b)**.**

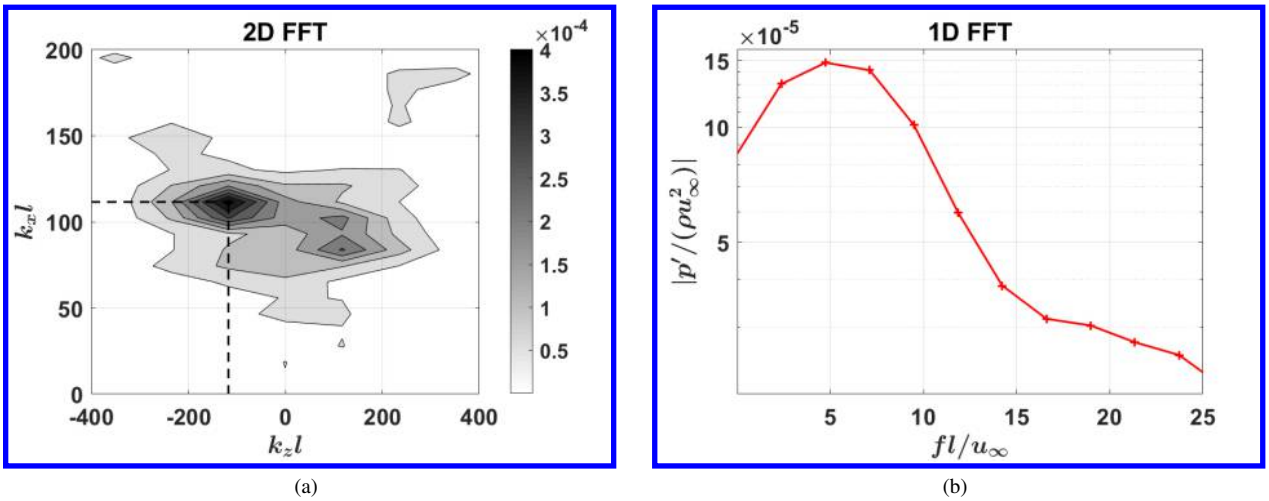

(a) (b)

Fig. 6 Spectral signature of pressure disturbances. (a) **Streamwise-spanwise frequencies corresponding to mode in fig. 5(c). The most amplified wavenumber pair** (k_x, k_z) **is highlighted.** (b) **Amplitude of pressure temporal spectrum at** $(x/l, z/l) = (0.9, 0.14)$ **in fig. 4.**

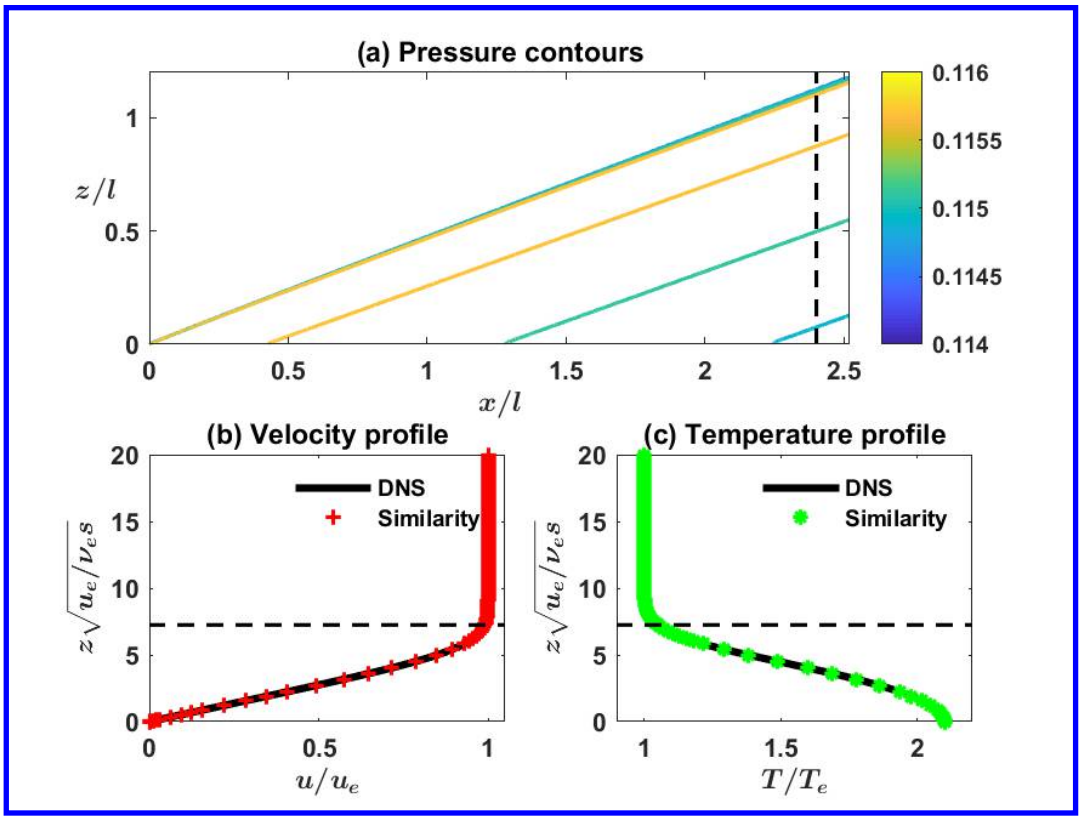

Fig. 7 Steady base flow features of supersonic flat plate at adiabatic wall conditions. The DNS flow field is compared with self-similar profiles of velocity (b) and temperature (c) at $x/l = 2.4$, marked in (a). Horizontal dashed line $(--)$ denotes boundary layer edge in (b, c).

V. Flat plate transition induced by tunnel disturbances

A. Laminar steady base flow and boundary conditions

To study the effects of tunnel disturbances on a test object, a zero-thickness supersonic adiabatic flat plate configuration is considered. The length of the flat plate is 500 mm, with the freestream conditions corresponding to the supersonic tunnel outlined in sec. III. To generate the steady base flow, a $2D$ rectangular computational domain is considered such that the upper boundary includes the shock emanating from the leading edge. On the wall (lower boundary) no slip conditions are specified with isothermal wall temperature. At the inlet (left boundary) and upper boundary freestream conditions $(u = 1, v = 0, P = 1/(\gamma M^2), \rho = 1)$ are specified. At the exit (left boundary) a zero-gradient condition is specified for all the field variables. The computational domain is discretized with 3004×400 grid points in streamwise and wall-normal directions, respectively. The near wall grid-spacing is $z/l = 1 \times 10^{-4}$ and is stretched exponentially to the freestream. In the streamwise direction, a uniform grid spacing is employed, except at the exit where the grid has been stretched to dampen acoustic reflections. This stretching is applied over a length of 10 mm with 4 points and the corresponding flow features are discarded. Navier-Stokes equations are solved over this domain as described in sec. II till convergence is achieved.

Figure 7 shows the steady base flow features of the supersonic flat plate described above. Pressure contours in fig. 7(a) show a weak shock emanating from the leading edge and delineating into a Mach wave at 24 deg angle with the flat plate. For transition studies, the residual error of base flow must be orders of magnitude smaller than the perturbations. To verify the convergence, the base flow is compared with compressible Blasius solutions. Corresponding to the location $x/l = 2.4$ marked in fig. 7(a), the DNS streamwise velocity and temperature are validated with self-similar profiles in fig. 7(b,c), which shows excellent agreement. Also, the zero gradient of wall temperature can be noticed from fig. 7(c). To study the effect of tunnel disturbances on this flat plate, the current $2D$ domain is extruded in $y-$direction, extending from $y/l = 0$ to $y/l = 0.135$, with 201 uniformly spaced grid points. The boundary conditions to emulate

transition to turbulence from tunnel spectra are elucidated next.

As noted in sec. IV, the freestream tunnel noise has predominantly slow acoustic nature. For a unit vector $\bar{x} = xsin(\theta_1)sin(\theta_2) + zsin(\theta_1)cos(\theta_2) + ycos(\theta_2)$, the slow acoustic wave relations are given as in eq. 14.

$$
\begin{aligned}
u' &= -M \sum_{i=1}^{nf} A_i sin(\theta_{1,i}) sin(\theta_{2,i}) cos(k_{x,i}x + k_{y,i}y + k_{z,i}z - \omega_i t + \phi_i) \\
v' &= -M \sum_{i=1}^{nf} A_i cos(\theta_{2,i}) cos(k_{x,i}x + k_{y,i}y + k_{z,i}z - \omega_i t + \phi_i) \\
w' &= -M \sum_{i=1}^{nf} A_i cos(\theta_{1,i}) sin(\theta_{2,i}) cos(k_{x,i}x + k_{y,i}y + k_{z,i}z - \omega_i t + \phi_i) \\
p' &= \sum_{i=1}^{nf} A_i cos(k_{x,i}x + k_{y,i}y + k_{z,i}z - \omega_i t + \phi_i) \\
\rho' &= M^2 \sum_{i=1}^{nf} A_i cos(k_{x,i}x + k_{y,i}y + k_{z,i}z - \omega_i t + \phi_i)
\end{aligned}
\tag{14}
$$

The details of extracting the number of modes nf, spectral content (k_x, k_y, k_z, ω) and the amplitudes A_i have been outlined in sec. IV. The phase $\phi_i \in [-\pi, \pi]$ has been generated randomly using FORTRAN pseudo-random number function, to emulate a realistic phase relation among the waves. These disturbances are imposed in the freestream at the inlet (left boundary) to include the leading edge shock, and the freestream (top boundary). The domain is periodic in the spanwise direction.

The leading edge shock plays a vital role in receptivity of freestream disturbances [41]. Interaction of acoustic waves with a shock generates acoustic, vortical, entropic fluctuations [42]. To highlight the interplay between the leading edge shock and the freestream disturbances, transition induced by oblique (spanwise) waves with zero angle of (wall-normal) inclination, similar to earlier studies [8, 43], are next presented.

B. Transitional flow features

As mentioned earlier, supersonic LTT involves receptivity and linear growth of disturbances, followed by non-linear saturation and breakdown to turbulence. One of the ways to visualize this process is to examine the evolution of vortical structures during transition. Here, these structures are extracted with the Q- criterion, which is defined as the second-invariant of the tensor $Q = 0.5[|\Omega|^2 - |\mathbf{S}|^2]$, where Ω and $\mathbf{S}$ are antisymmetric and symmetric components of velocity-gradient [44]. In fig. 8 these iso-surfaces are highlighted in three increments and are colored by streamwise velocity. Randomly aligned oblique waves due the freestream forcing are evident in fig. 8(a) ($Q = 10$) for $0.12 < x < 0.9$. This is the signature of amplifying unstable oblique first-mode waves in supersonic flows. At the end of this subdomain, secondary instabilities develop on the most unstable first-mode waves and is observed as a precursor to oblique *lambda*-vortices. The nature of these secondary instabilities is not apparent in the current visualization due to multiple potentially interacting unstable waves and will be discussed through higher-order spectral analysis. Figure 8(b) highlights the vortical structures in the range $0.9 < x < 1.67$ at $Q = 100$. Streamwise streaks are evident at the center of the domain with high-frequency structures over them. These structures are intermittent and the corresponding leading and trailing edges convect at different velocities, and the signature of such earlier structure is observed at the end of this subdomain. In fig. 8(c) for $1.67 < x < 2.45$ and $Q = 100$, onset of early turbulent regime is observed with vortical structures at multiple scales.

To further examine the nature of disturbance evolution, instantaneous streamwise velocity fluctuation (deviation from laminar base flow) fields are plotted in fig. 9. Closer to the wall ($z/l = 3 \times 10^{-4}$) in fig. 9(a) at $x/l = 1.5$ low-speed streaks (colored in blue) of smaller spanwise wavelength than high-speed streaks (colored in red) are observed. These streaks correspond to those highlighted in fig. 8(b). Further downstream, for $x > 1.75$, asymmetric oscillations of low-speed streaks (see $(x/l, y/l) \sim (1.75 - 2.0, 0.05)$) and their breakdown are observed. Such oscillations of low-speed streaks are observed throughout the late non-linear stages of transition corresponding to fig. 9(c). The high-speed streaks are interspersed among the low-speed streaks in $1.75 < x < 2.45$. The nature of their instability cannot be discerned from the coherent structures alone and will be further examined in the future work. Streamwise velocity fluctuations at the wall-normal location $z/l = 5 \times 10^{-3}$ are depicted in fig. 9(b). The signature of oblique waves is observed for

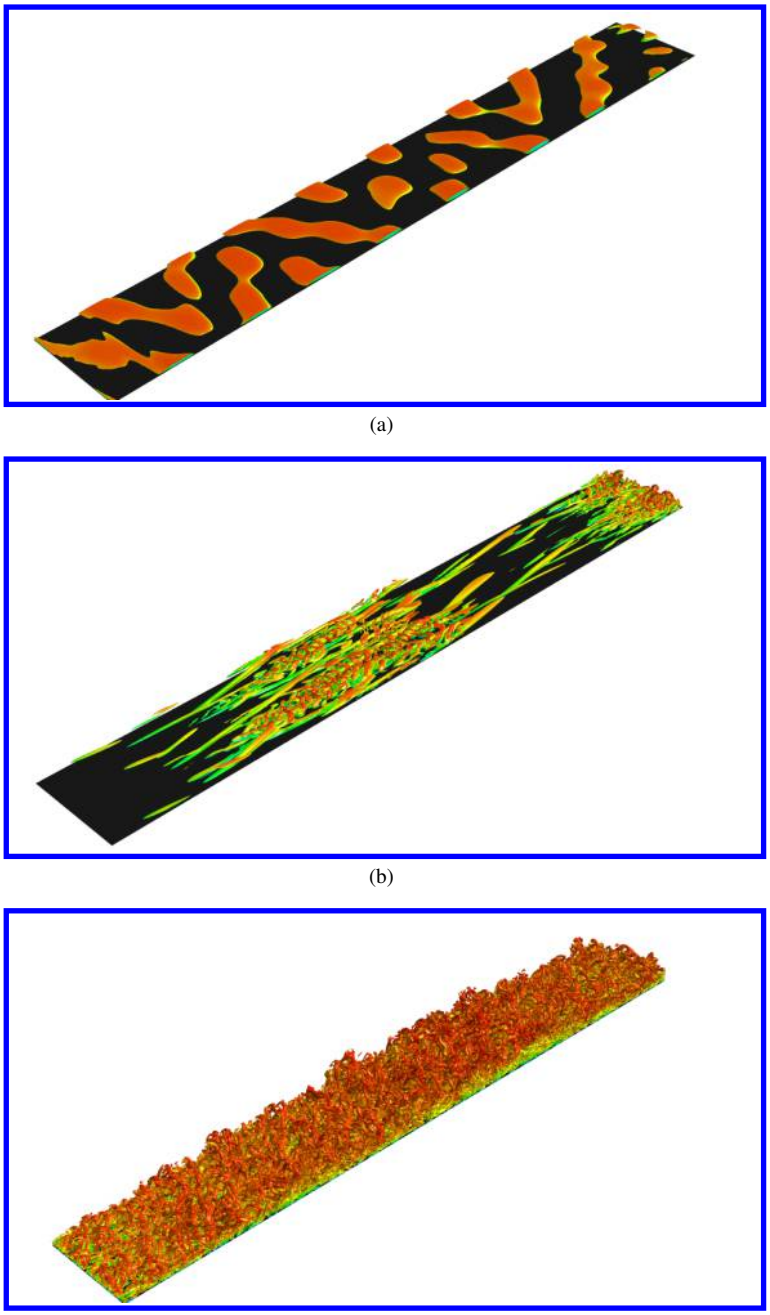

(a)

(b)

(c)

Fig. 8 Instantaneous vortical structures identified by Q-criterion, colored by streamwise velocity. (a) $Q = 10$ **in** $0.12 < x < 0.9$ (b) $Q = 100$ **in** $0.9 < x < 1.67$ (c) $Q = 100$ **in** $1.67 < x < 2.45$**.**

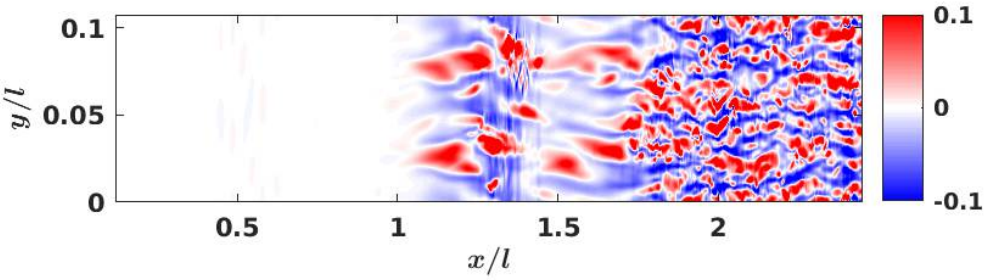

(a)

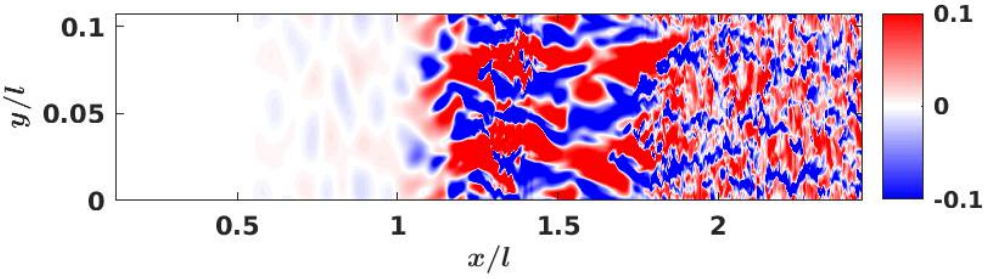

(b)

Fig. 9 Instantaneous streamwise velocity perturbation contours at $(a)\ z/l = 3 \times 10^{-4}$ $(b)\ z/l = 5 \times 10^{-3}$**.**

$0.5 < x < 1.0$ and the fluctuations are intense (compared to near wall in fig. 9(a)) in $1.25 < x < 1.75$, suggesting stronger perturbations closer to the boundary-layer edge. The streaky structures are less evident for $x > 2.0$, highlighting that the predominant activity of flow instabilities is closer the boundary-layer edge (near generalized inflection point) in early transitional regime, and moves near wall in the late non-linear stages. The latter can be partly attributed to the self-sustaining mechanism of early turbulent onset regime [45].

The wall-normal density gradient magnitude (pseudo-Schlieren) at the symmetry plane ($y/l = 0.05$) at two time instances are highlighted in fig. 10. At the non-dimensional time instants $t = 7.0$,9.0, the signature of perturbation evolution is strongest closer to the boundary-layer edge for $0.5 < x < 1.0$ in fig. 10(a,b). Stronger high-frequency fluctuations from near wall to boundary-layer edge are evident in fig. 10(a) for $1.0 < x < 1.5$, corresponding to those in fig. 8(b). Further downstream for $1.75 < x < 2.45$, intense fluctuations near-wall and freestream radiation like signature is observed, denoting onset of early turbulence. The intermittent nature of fluctuations is evident from the difference in perturbation signature at $x/l \sim 1.25$ in fig. 10(b) compared to that in fig. 10(a). Also, the extent of early turbulent regime is longer at $t = 9.0$ in the range $1.5 < x < 2.45$, suggesting merging of intermittent turbulent spots in the late transitional regime. This intermittency can be attributed to the random phase angles in the freestream spectra and cannot be captured by only deterministic forcing of the unstable waves.

The non-stationarity of the disturbances is examined using scalogram of temperature perturbations at the boundary-layer edge. To this end, temporal signal with 1×10^5 points were collected after 5 time periods of the smallest inlet frequency, at time step $\Delta t = 1 \times 10^{-4}$. The data is processed using Morlet wavelet as it is more efficient in resolving scale distributions [46], and the spectral distribution is highlighted in fig. 11. In the early transitional regime, at $x/l = 0.66$ in fig. 11(a), the frequency (fl/u_∞) signature is observed throughout the forcing period, and is maximum at for $fl/u_\infty < 15$ based on the inlet forcing. Further downstream at $x/l = 1.33$, the lower frequency fluctuations ($fl/u_\infty < 10$) are predominant throughout the forcing period, corresponding to the streaky structures in fig. 9. Intensification of higher frequency waves ($fl/u_\infty > 15$) with varying amplification levels is also noticed, confirming to the intermittency in the density gradient evolution in fig. 10. In experimental transition studies by white-noise excitation in incompressible flows, Shaikh [46] also reported such intermittent high-frequency fluctuations. At $x/l = 2.0$ in fig. 11(c), spectral filling is observed, indicating late non-linear stages of transition.

To investigate the phase-coupled interactions leading to spectral filling discussed in fig. 11, bispectral analysis [47]

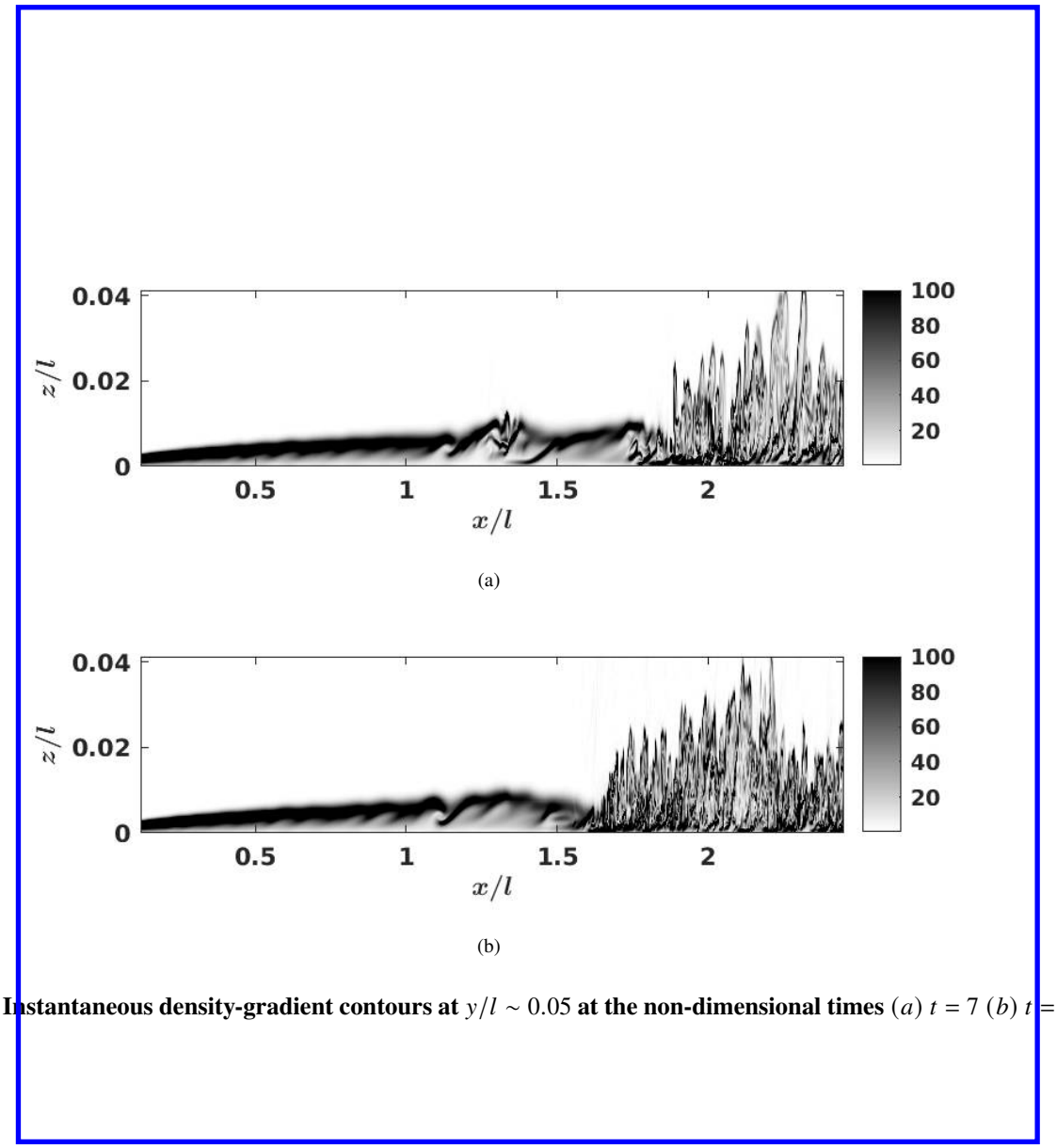

Fig. 10 Instantaneous density-gradient contours at $y/l \sim 0.05$ at the non-dimensional times (a) $t = 7$ (b) $t = 9$.

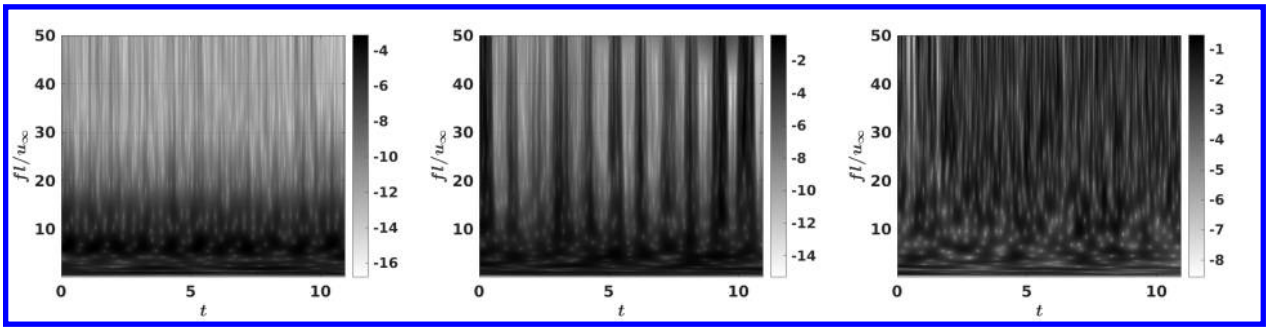

Fig. 11 Scalogram of temperature fluctuations (logarithmic scale) depicting non-dimensional frequencies (fl/u_∞) with time (t) at the laminar boundary-layer edge at (a) $x/l = 0.66$ (b) $x/l = 1.33$ (b) $x/l = 2.0$.

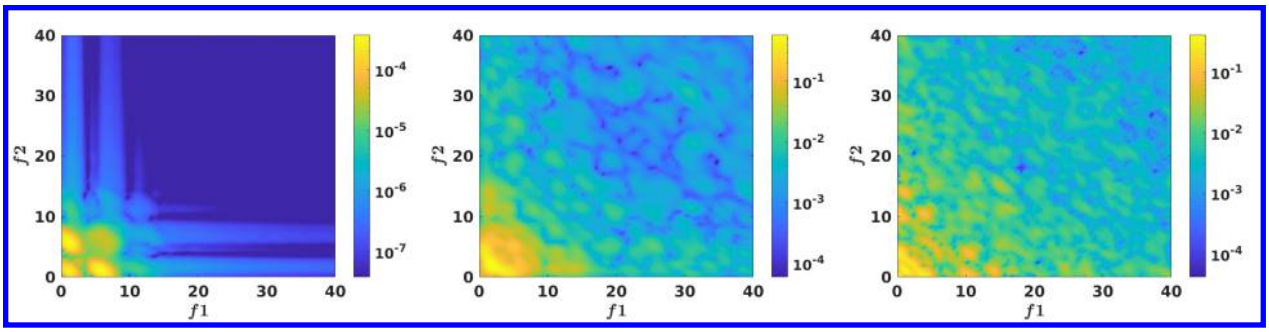

(a) (b) (c)

Fig. 12 Bicoherence of temperature fluctuations depicting interactions of frequencies $f1 = f_1 l/u_\infty$, $f2 = f_2 l/u_\infty$ at the laminar boundary layer edge at $(a)\ x/l = 0.66$ $(b)\ x/l = 1.33$ $(b)\ x/l = 2.0$

is employed. The bispectrum $B(f_1, f_2)$ indicates the extent to which phases among three waves at frequencies f_1, f_2, and $(f_1 + f_2)$ are nonlinearly coupled, and is defined by eq. 15

$$B(f_1, f_2) = E[A(f_1)A(f_2)A^{\dagger}(f_1 + f_2)] \tag{15}$$

where E is the expectation operator, $A(f_1)$ is the discrete Fourier amplitude of the f_1 component, and the superscript † stands for the complex conjugate. Bicoherence is extracted by dividing temperature perturbation signal (corresponding to fig. 11) into 8 blocks with 50% overlap, and is depicted in fig. 12. In the early transitional regime at $x/l = 0.66$ in fig. 12(a), the disturbance at $f1 \sim 5$ interacts strongly with other first-mode lower frequencies in the inlet spectrum generating higher-frequencies. Stronger interactions among lower frequencies close to $f1 \sim 1$ is also observed, resulting in the spectral distribution in fig. 11(a). The lower frequency interactions are predominant at $x/l = 1.33$ in fig. 12(b) corresponding to the streaky structures in fig. 8(b). Stronger interactions of higher frequency waves $f1 \sim 15$ with lower frequencies $f2 \sim 0$ are also observed, and the shorter wavelength signature over the streaks in fig. 8(b) can be attributed to their interplay. The instability mechanism behind these coherent structures will be further explored in future studies. Multi-scale interactions are observed in the late-transitional regime in fig. 12(c) corresponding to the fine scale structures in fig. 8(c).

As noted earlier, it is vital to characterize the laminar-turbulent onset point on supersonic flight vehicle. For high speed flows, the definition of transition location is not unique, and different methods used in experiments do not always agree [48]. Different definitions of transition are employed computationally, mainly based on skin friction coefficient, wall heat transfer rate, boundary layer thickness measurements and spanwise turbulent spectrum [7]. In the current work, we use the skin friction coefficient to characterize the transition location, which is used commonly in experiments. The skin friction (C_f) can be estimated from the flow field using relation 16, and the flow regime can be characterized by comparing it with the deviation from the corresponding laminar flow value (C_{fL}).

$$C_f = \frac{2\tau_w}{\rho_e U_e^2 Re} \tag{16}$$

$$C_{fL} = \frac{0.664}{\sqrt{Re_x/(\rho^R \mu^R)}} \tag{17}$$

where a reference temperature $T^R = T_e + 0.5(T_w - T_e) + 0.22(T_{ad} - T_e)$ is used to calculate the density (ρ^R) and the viscosity (μ^R) used in the correlation [49].

The span and time-averaged skin-friction coefficient profile of the transitional flow is plotted in fig. 13(a) along with the empirical laminar and turbulent correlations. Following an initial reduction till $x \sim 1.0$, the skin friction coefficient deviates from the laminar correlation indicating onset of transition. This deviation corresponds to the streak formation regime in fig. 8(b). The friction coefficient increases monotonically till $x \sim 1.9$ till the turbulent correlation and approximately saturates. For $x > 2.0$ the flow is in early turbulent regime, characterized by the preponderance of hairpin vortices in fig. 8(c) and freestream radiation in fig. 10.

To investigate the establishment of equilibrium turbulence, the time-averaged development of streamwise velocities (at $y/l \sim 0.05$) are plotted using scaled wall-units, u^+ and z^+ in fig. 13(b). The compressibility effects are accounted to

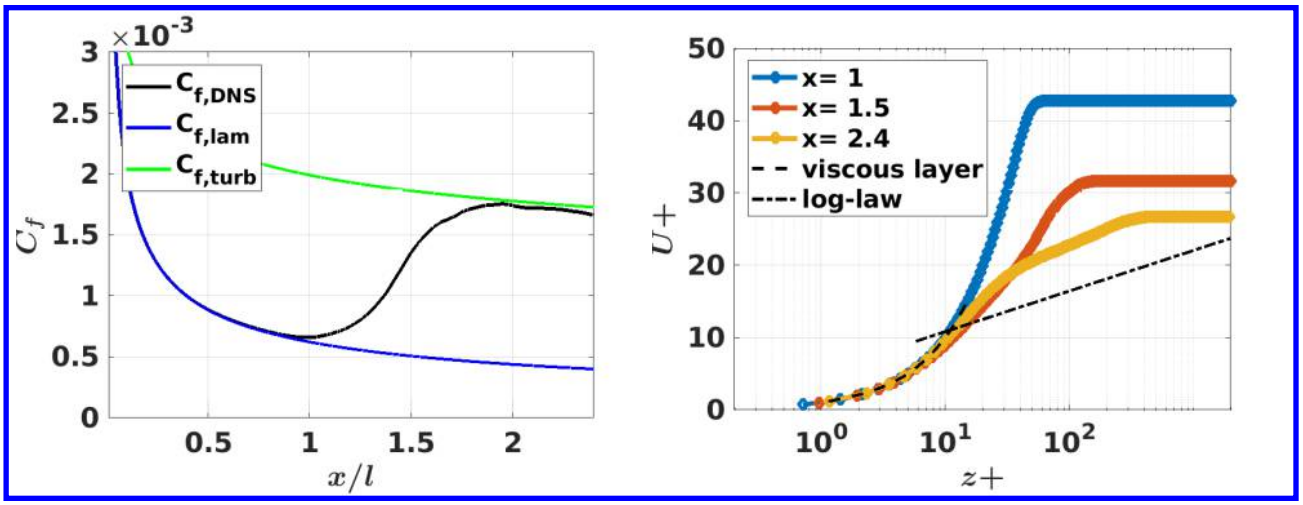

(a) (b)

Fig. 13 Flow features highlighting onset of turbulence. (a) **Span- and time-averaged skin-friction coefficient, compared with empirical laminar and turbulent correlations.** (b) **Streamwise development of equilibrium turbulent velocity profile through van Driest transformation at** $y/l \sim 0.05$**.**

obtain van Driest transformed velocity profile, and the viscous and log-layers are depicted by dashed and dashed-dotted lines, respectively. While the characteristic of viscous sub-layer is linear relation between u^+ and z^+, log-layer represents a fully turbulent flow. The viscous sub-layer extends till $z^+ \sim 10$ at $x/l = 1.5$, consistent with earlier supersonic transition studies ([6]). Progression of flow from $x = 1.0$ to $x = 2.4$ indicates the onset of early turbulent features but not the development of equilibrium turbulence.

VI. Summary

Turbulence is generated in a double-walled configuration at Mach 2.5 and isothermal wall conditions (adiabatic temperature) at a unit Reynolds number $4.9 \times 10^6/m$. A reduced order representation of freestream slow acoustic disturbances is developed using data-driven techniques including POD, CDMD. Transition to turbulence is studied on a laminar adiabatic flat plate, at the freestream tunnel conditions, with the inlet disturbances from the reduced order modeling. The freestream perturbations synchronize with the boundary layer and linear instabilities are triggered. In the initial transitional regime, randomly oriented oblique first-modes are generated. These disturbances evolve exponentially and develop further secondary instabilities.

The most amplified linear instability mode in the spectrum interacts with other waves in the freestream and streamwise vortices are generated. This marks the onset of the friction coefficient deviation from the laminar value. Intermittent high-frequency structures develop over the streamwise streaks which merge downstream leading to form early turbulent regime. This regime is characterized by low-speed streaks near wall of smaller spanwise wavenumber than during early stages of transition, and oscillate asymmetrically. Multiple hairpin vortices and freestream radiation of perturbations have also been observed. Here, while the wall skin-friction coefficient approaches the turbulent correlation, the self-similar turbulent velocity profile indicates developing turbulence. In future work, the role of freestream wave inclination and nature of secondary instabilities leading to turbulence onset will be further explored.

Acknowledgments

This research was supported by the Office of Naval Research (Grant: N00014-21-1-2408) monitored by E. Marineau with R. Burnes as technical point of contact. The authors (Yuchen Liu and Lian Duan) would also like to acknowledge financial support by the the National Science Foundation (under grant CBET 2001127, managed by Dr. Ron Joslin). Discussions with Dr. M. Choudhari are gratefully acknowledged. The simulations were carried out using resources provided by the U.S. Department of Defense High Performance Computing Modernization Program and the Ohio Supercomputer Center. Several figures were made using FieldView software with licenses obtained from the Intelligent

Light University Partnership Program.

References

[1] Fedorov, A., and Tumin, A., "High-speed boundary-layer instability: old terminology and a new framework," *AIAA journal*, Vol. 49, No. 8, 2011, pp. 1647–1657.

[2] Schneider, S. P., "Development of hypersonic quiet tunnels," *Journal of Spacecraft and Rockets*, Vol. 45, No. 4, 2008, pp. 641–664.

[3] Schneider, S. P., "Effects of High-Speed Tunnel Noise on Laminar-Turbulent Transition," *Journal of Spacecraft and Rockets*, Vol. 38, No. 3, 2001, pp. 323–333.

[4] Laufer, J., "Some statistical properties of the pressure field radiated by a turbulent boundary layer," *The Physics of Fluids*, Vol. 7, No. 8, 1964, pp. 1191–1197.

[5] Schneider, S. P., "Effects of high-speed tunnel noise on laminar-turbulent transition," *Journal of Spacecraft and Rockets*, Vol. 38, No. 3, 2001, pp. 323–333.

[6] Mayer, C. S., Wernz, S., and Fasel, H. F., "Numerical investigation of the nonlinear transition regime in a Mach 2 boundary layer," *Journal of fluid mechanics*, Vol. 668, 2011, p. 113.

[7] Franko, K. J., and Lele, S. K., "Breakdown mechanisms and heat transfer overshoot in hypersonic zero pressure gradient boundary layers," *Journal of Fluid Mechanics*, Vol. 730, 2013, pp. 491–532.

[8] Balakumar, P., and Chou, A., "Transition prediction in hypersonic boundary layers using receptivity and freestream spectra," *AIAA Journal*, Vol. 56, No. 1, 2018, pp. 193–208.

[9] Marineau, E. C., Moraru, G. C., Lewis, D. R., Norris, J. D., Lafferty, J. F., Wagnild, R. M., and Smith, J. A., "Mach 10 boundary layer transition experiments on sharp and blunted cones," *19th AIAA International Space Planes and Hypersonic Systems and Technologies Conference*, 2014, p. 3108.

[10] Hader, C., and Fasel, H. F., "Towards simulating natural transition in hypersonic boundary layers via random inflow disturbances," *Journal of Fluid Mechanics*, Vol. 847, 2018.

[11] Goparaju, H., and Gaitonde, D. V., "Transition to turbulence on hypersonic flat plates induced by stochastic forcing," *AIAA Scitech 2021 Forum*, 2021, p. 1738.

[12] Dettenrieder, F., Sullivan, B. T., Schöneich, A. G., Laurence, S. J., and Bodony, D. J., "Direct Numerical Simulation of Boundary Layer Receptivity to Acoustic Radiation in a Hypersonic Compression Ramp Flow," *AIAA Scitech 2021 Forum*, 2021, p. 0368.

[13] Pate, S. R., "Effects of wind tunnel disturbances on boundary-layer transition with emphasis on radiated noise: a review," Tech. rep., ARO INC ARNOLD AFS TN, 1980.

[14] Duan, L., Choudhari, M., and Wu, M., "Numerical study of acoustic radiation due to a supersonic turbulent boundary layer," *Journal of Fluid Mechanics*, Vol. 746, 2014, p. 165.

[15] Duan, L., Choudhari, M. M., and Zhang, C., "Pressure Fluctuations Induced by a Hypersonic Turbulent Boundary Layer," *Journal of Fluid Mechanics*, Vol. 804, 2016, pp. 578–607.

[16] Zhang, C., Duan, L., and Choudhari, M. M., "Effect of wall cooling on boundary-layer-induced pressure fluctuations at Mach 6," *Journal of Fluid Mechanics*, Vol. 822, 2017, pp. 5–30.

[17] Zhang, C., and Duan, L., "Acoustic radiation from a mach 14 turbulent boundary layer," *54th AIAA Aerospace Sciences Meeting*, 2016, p. 0048.

[18] Huang, J., and Duan, L., "Direct numerical simulation of acoustic noise generation from the nozzle wall of a hypersonic wind tunnel," *47th AIAA Fluid Dynamics Conference*, 2017, p. 3631.

[19] Hildebrand, N., Choudhari, M. M., and Duan, L., "Direct Numerical Simulations of Acoustic Disturbances in Various Rectangular Nozzle Configurations," *AIAA Scitech 2020 Forum*, 2020, p. 0587.

[20] Deegan, C. P., Duan, L., and Choudhari, M. M., "Direct Numerical Simulation of Acoustic Disturbances in the Rectangular Test Section of a Hypersonic Wind Tunnel," *2018 Fluid Dynamics Conference*, 2018, p. 3219.

[21] Duan, L., Choudhari, M. M., Chou, A., Munoz, F., Radespiel, R., Schilden, T., Schröder, W., Marineau, E. C., Casper, K. M., Chaudhry, R. S., et al., "Characterization of freestream disturbances in conventional hypersonic wind tunnels," *Journal of spacecraft and rockets*, Vol. 56, No. 2, 2019, pp. 357–368.

[22] Kennedy, C. A., and Gruber, A., "Reduced aliasing formulations of the convective terms within the Navier–Stokes equations for a compressible fluid," *Journal of Computational Physics*, Vol. 227, No. 3, 2008, pp. 1676–1700.

[23] Pirozzoli, S., "Generalized conservative approximations of split convective derivative operators," *Journal of Computational Physics*, Vol. 229, No. 19, 2010, pp. 7180–7190.

[24] Pirozzoli, S., "Stabilized non-dissipative approximations of Euler equations in generalized curvilinear coordinates," *Journal of Computational Physics*, Vol. 230, No. 8, 2011, pp. 2997–3014.

[25] Williamson, J., "Low-storage runge-kutta schemes," *Journal of Computational Physics*, Vol. 35, No. 1, 1980, pp. 48–56.

[26] Xu, S., and Martin, M. P., "Assessment of inflow boundary conditions for compressible turbulent boundary layers," *Physics of Fluids*, Vol. 16, No. 7, 2004, pp. 2623–2639.

[27] Prasad, C., Huang, J., Duan, L., and Gaitonde, D. V., "On the Nature of Freestream Disturbances in a Two-Dimensional Supersonic Test Section," *AIAA Scitech 2021 Forum*, 2021, p. 0162.

[28] Balsara, D. S., and Shu, C.-W., "Monotonicity preserving weighted essentially non-oscillatory schemes with increasingly high order of accuracy," *Journal of Computational Physics*, Vol. 160, No. 2, 2000, pp. 405–452.

[29] Ducros, F., Ferrand, V., Nicoud, F., Weber, C., Darracq, D., Gacherieu, C., and Poinsot, T., "Large-eddy simulation of the shock/turbulence interaction," *Journal of Computational Physics*, Vol. 152, No. 2, 1999, pp. 517–549.

[30] Lele, S. K., "Compact finite difference schemes with spectral-like resolution," *Journal of computational physics*, Vol. 103, No. 1, 1992, pp. 16–42.

[31] Visbal, M. R., and Gaitonde, D. V., "On the use of higher-order finite-difference schemes on curvilinear and deforming meshes," *Journal of Computational Physics*, Vol. 181, No. 1, 2002, pp. 155–185.

[32] Beam, R. M., and Warming, R., "An implicit factored scheme for the compressible Navier-Stokes equations," *AIAA journal*, Vol. 16, No. 4, 1978, pp. 393–402.

[33] Pulliam, T. H., and Chaussee, D., "A diagonal form of an implicit approximate-factorization algorithm," *Journal of Computational Physics*, Vol. 39, No. 2, 1981, pp. 347–363.

[34] Lee, J.-H., and Sung, H. J., "Structures in turbulent boundary layers subjected to adverse pressure gradients," *Journal of fluid mechanics*, Vol. 639, 2009, p. 101.

[35] Smits, A., Matheson, N., and Joubert, P., "Low-Reynolds-number turbulent boundary layers in zero and favorable pressure gradients," *Journal of ship research*, Vol. 27, No. 03, 1983, pp. 147–157.

[36] Pirozzoli, S., and Bernardini, M., "Turbulence in supersonic boundary layers at moderate Reynolds number," *Journal of Fluid Mechanics*, Vol. 688, 2011, pp. 120–168.

[37] Van Driest, E. R., "Turbulent boundary layer in compressible fluids," *Journal of the Aeronautical Sciences*, Vol. 18, No. 3, 1951, pp. 145–160.

[38] Schmid, P. J., Henningson, D. S., and Jankowski, D., "Stability and transition in shear flows. Applied mathematical sciences, Vol. 142," *Appl. Mech. Rev.*, Vol. 55, No. 3, 2002, pp. B57–B59.

[39] Taira, K., Brunton, S. L., Dawson, S. T., Rowley, C. W., Colonius, T., McKeon, B. J., Schmidt, O. T., Gordeyev, S., Theofilis, V., and Ukeiley, L. S., "Modal analysis of fluid flows: An overview," *Aiaa Journal*, Vol. 55, No. 12, 2017, pp. 4013–4041.

[40] Sayadi, T., Schmid, P. J., Nichols, J. W., and Moin, P., "Reduced-order representation of near-wall structures in the late transitional boundary layer," *Journal of fluid mechanics*, Vol. 748, 2014, pp. 278–301.

[41] Egorov, I., Sudakov, V., and Fedorov, A., "Numerical modeling of perturbation propagation in a supersonic boundary layer," *Fluid Dynamics*, Vol. 39, No. 6, 2004, pp. 874–884.

[42] Duck, P. W., Lasseigne, D. G., and Hussaini, M., "On the interaction between the shock wave attached to a wedge and freestream disturbances," *Theoretical and Computational Fluid Dynamics*, Vol. 7, No. 2, 1995, pp. 119–139.

[43] Cerminara, A., and Sandham, N., "Transition mechanisms in cross-flow-dominated hypersonic flows with free-stream acoustic noise," *Journal of Fluid Mechanics*, Vol. 896, 2020.

[44] Jeong, J., and Hussain, F., "On the identification of a vortex," *Journal of fluid mechanics*, Vol. 285, 1995, pp. 69–94.

[45] Schoppa, W., and Hussain, F., "Coherent structure generation in near-wall turbulence," *Journal of fluid Mechanics*, Vol. 453, 2002, pp. 57–108.

[46] Shaikh, F., "Investigation of transition to turbulence using white-noise excitation and local analysis techniques," *Journal of Fluid Mechanics*, Vol. 348, 1997, pp. 29–83.

[47] Kim, Y. C., and Powers, E. J., "Digital bispectral analysis and its applications to nonlinear wave interactions," *IEEE transactions on plasma science*, Vol. 7, No. 2, 1979, pp. 120–131.

[48] Stetson, K., and Kimmel, R., "On the breakdown of a hypersonic laminar boundary layer," *31st Aerospace Sciences Meeting*, 1993, p. 896.

[49] Eckert, E., "Engineering relations for friction and heat transfer to surfaces in high velocity flow." *AIAA Journal*, Vol. 41, No. 7, 2003, pp. 256–258.